ADVANCED MATERIALS
www.advmat.de

Graphene Readout Silicon-Based Microtube Photodetectors for Encrypted Visible Light Communication

Ziyu Zhang, Tianjun Cai, Zengxin Li, Binmin Wu, Zhi Zheng, Chunyu You, Guobang Jiang, Mingze Ma, Zengyi Xu, Chao Shen,* Xiang-zhong Chen, Enming Song, Jizhai Cui, Gaoshan Huang, and Yongfeng Mei**

The implementation of an advanced light receiver is imperative for the widespread application of visible light communication. However, the integration of multifunctional and high-performance visible light receivers is still limited by device structure and system complexity. Herein, a graphene-readout silicon-based microtube photodetector is proposed as the receiver for omnidirectional Mbps-level visible light communication. The integration of graphene-semiconductor material systems simultaneously ensures the effective absorption of incident light and rapid readout of photogenerated carriers, and the device exhibits an ultrafast response speed of 75 ns and high responsivity of 6803 A W^{-1}. In addition, the microtube photodetector realizes the omnidirectional light-trapping and enhanced polarization photodetection. As the receiving end of the visible light communication system, the microtube photodetector achieves a data rate of up to 778 Mbps, a field of view of 140°, and the encrypted visible light communication of polarized light, providing a new possibility for the future development of the internet of things and information security.

1. Introduction

Visible light communication (VLC), a recently developed communication method with high speed, anti-electromagnetic interference, and a wide range of spectrum resources, has found widespread use in underwater communication,[1] data broadcasting,[2] intelligent devices,[3] and encrypted transmission.[4] Among them, the photodetector, as the signal receiver, has a pivotal influence on the data rate, communication range, etc.[5] The wider field of view (FOV) of the signal receiver will enhance communication coverage and stability, and the function of multi-optical information communication can further enhance information density and security.[6] At present, high-performance VLC detectors have been widely studied. The receiving end of VLC typically uses a p-i-n diode[5c,7] and an avalanche photodiode.[8] However, these planar devices generally struggle to achieve wide-angle reception. Additional complex CMOS processes are required for the fabrication of multi-dimensional optical information devices.[6d,9] Therefore, the macroscopic receiving array and additional optical path conditions are mainly employed in VLC receivers,[6b,c] which significantly restrict the transmission efficiency and application of VLC. The future development of VLC urgently requires on-chip

Z. Zhang, T. Cai, Z. Zheng, C. You, G. Jiang, M. Ma, J. Cui, G. Huang, Y. Mei
Department of Materials Science & State Key Laboratory of Molecular Engineering of Polymer
Fudan University
Shanghai 200438, China
E-mail: yfm@fudan.edu.cn

Z. Li, Z. Xu, C. Shen
Key Laboratory for Information Science of Electromagnetic Waves
Department of Communication Science and Engineering
Fudan University
Shanghai 200438, China
E-mail: chaoshen@fudan.edu.cn

B. Wu
State Key Laboratory of Infrared Physics
Shanghai Institute of Technical Physics
Chinese Academy of Sciences
Shanghai 200083, China
E-mail: wubinmin@mail.sitp.ac.cn

The ORCID identification number(s) for the author(s) of this article can be found under https://doi.org/10.1002/adma.202413771

DOI: 10.1002/adma.202413771

X.-zhong Chen, E. Song, G. Huang, Y. Mei
Shanghai Frontiers Science Research Base of Intelligent Optoelectronics and Perception
Institute of Optoelectronics
Fudan University
Shanghai 200438, China

X.-zhong Chen, G. Huang, Y. Mei
Fudan University
Yiwu, Zhejiang 322000, China

X.-zhong Chen, E. Song, J. Cui, G. Huang, Y. Mei
International Institute of Intelligent Nanorobots and Nanosystems
Fudan University
Shanghai 200438, China

X.-zhong Chen, G. Huang
State Key Laboratory of Photovoltaic Science and Technology
Fudan University
Shanghai 200438, China

integration devices that are free of additional optical components, which also meet the needs of miniaturized communication components, large receiving areas, and multi-dimensional light information transmission.

Nanomembranes, as a material system with excellent flexibility and semiconductor process compatibility,[10] can be greatly deformed by the strained layer in the thickness direction and assembled into 3D structures.[11] With appropriate design, self-assembled 3D nanomembranes are capable to achieve effective photodetection.[12] Based on the anisotropic microstructure, the self-rolled nanomembrane microtube structures have realized omnidirectional visible light photodetectors without additional optical components.[12a,e] In our previous work, the potential of polarization photodetection in silicon (Si) nanomembrane microtubes is observed and discussed.[12a,13] However, self-rolled nanomembrane visible photodetectors still face challenges such as poor responsivity of nanomembranes with small thickness and slow response time due to interface defects and low material mobility.[11a] In addition, it is still difficult to achieve efficient polarization photodetection only by the anisotropy of microstructures, which can hardly meet the fast and sensitive response in high-speed VLC.

In this article, we introduce a design concept of graphene (Gr)-readout silicon germanium (SiGe)/Si nanomembrane microtube photodetector for wide-angle encrypted VLC. Through transmission electron microscopy (TEM) analysis of the cross section of the microtube, we confirm the non-destructive nature of the self-rolled technique and the mechanism of the rolled-up technique. The Gr-readout layer is integrated into the semiconductor nanomembrane, ensuring the fast response and stability of the device. The Gr-readout SiGe/Si microtube photodetectors exhibit good ohmic contact over a wide voltage range, exhibit ultrafast response, and achieve sensitive and obvious photoresponse in the visible range. Subsequently, work function and electron density in the Gr/SiGe interface are investigated, revealing the complementarity between the photogenerating carrier and photogating effect in SiGe, and fast readout in the Gr layer. The microtube structure of the Gr-readout SiGe/Si photodetector realizes almost omnidirectional on-chip photodetection and high dichroism ratio polarization detection via structure-material coupling. The microtube photodetector realizes hundreds-Mbps level VLC at both the on-off keying (OOK) and the discrete multi-tone (DMT) modulation modes and has a higher FOV (≈140°) compared to the planar photodetector (≈80°) at the same rate. In polarized VLC, encrypted communication can be realized according to the polarization state, revealing the application potential of the microtube photodetector in a miniaturized multifunctional optical communication receiver.

2. Results

The application fields of photodetectors play a crucial guiding role in the design of their devices and structures. In real-life scenarios, VLC can be practically applied in areas such as secure communication, wireless data transmission between devices, and smart home control.[3a,4a] To achieve efficient and reliable information transmission, a variety of receiving terminals in communication networks must be capable of responding to light signals from different angles in practical VLC applications (**Figure 1a**). Therefore, 3D photodetectors prepared using nanomembrane self-rolled technology will be able to make up for the functional limitations of planar detectors. As shown in Figure 1b, the Gr/SiGe/Si multilayer nanomembrane on Si substrate is assembled into a microtube structure via a self-rolled technique, which can be integrated on-chip for VLC. To achieve the fabrication of the microtube photodetector, we employed semiconductor-compatible photolithography, deposition, and sacrificial layer etching techniques, coupled with Gr wet transfer processes (Figures S1,S2, Supporting Information). Based on the process above, a wafer-scale microtube array can be fabricated, indicating the potential of mass production with high yield (Figure 1c). The SEM image of the photodetector array is shown in Figure 1d. A yield of 99.03% can be noticed at the center area of the wafer, confirming the device-level fabrication feasibility of this structural design and fabrication method (Figure 1d; Figure S3, Supporting Information). The self-rolling direction of the microtube structure can be selectively determined by the uniform strain and strain orientation of the epitaxial SiGe/Si nanomembrane along <100> direction, which allows large-scale and high-yield preparation of the photodetector with uniform diameter. Due to the lower Young's modulus of the <100> crystal orientation family in SiGe/Si nanomembranes compared to the <110> and <111> orientations, deformation is more likely to occur, making a pattern design parallel to this crystal orientation more conducive to the formation of tubular structures. Otherwise, microtube rupture or failure to form the tubular structure may occur (Figure S4, Supporting Information). In addition, the surface of the microtube structure is free of obvious stains and the channel is well-defined. Raman spectroscopy is used to characterize the strain distribution of the channel of the rolled-up Gr/SiGe/Si multilayer nanomembrane, and the Raman peaks of SiGe and Si showed obvious shifts, with the tensile strain determined to be 0.8% in Si and the compressive strain is −1.3% in SiGe, confirming the strain distribution along the thickness direction[14] (Figure S5, Note S1, Supporting Information). Planar nanomembrane photodetectors usually have low absorption rates due to their small thickness, where the absorption can be written as:[15] $A = 1 - e^{-\alpha t}$, where t is the thickness of the nanomembrane. Therefore, the design of micro-nano texture or additional reflective layers is required to compensate the shortcomings. Here, the assembly of a 3D microtube structure not only achieves the integrity of a photodetector with a smaller device footprint but also enhances the absorption in multilayer structures.[11a,12a] Optical finite element analysis can effectively evaluate the regulation of the photoresponse of the microtube structure. Here, the propagation path of linear optics in the microtube structure is simulated by the finite element method (Figure S6a, Supporting Information). When parallel light is incident, multiple reflections will occur inside the microtube, and several focal points may be formed to intensify the light in the tube cavity. In wave optics, the incident plane wave light on the microtube can form a high-intensity electric field norm region at a specific location, which indicates that the light is focused in the microtube cavity (Figure S6b, Supporting Information). Due to the multiple reflection and absorption of incident light in the microtube structure, the light can be trapped in the tubular photodetectors. If the focus position can be properly controlled, enhanced detection of light with the desired wavelength or certain

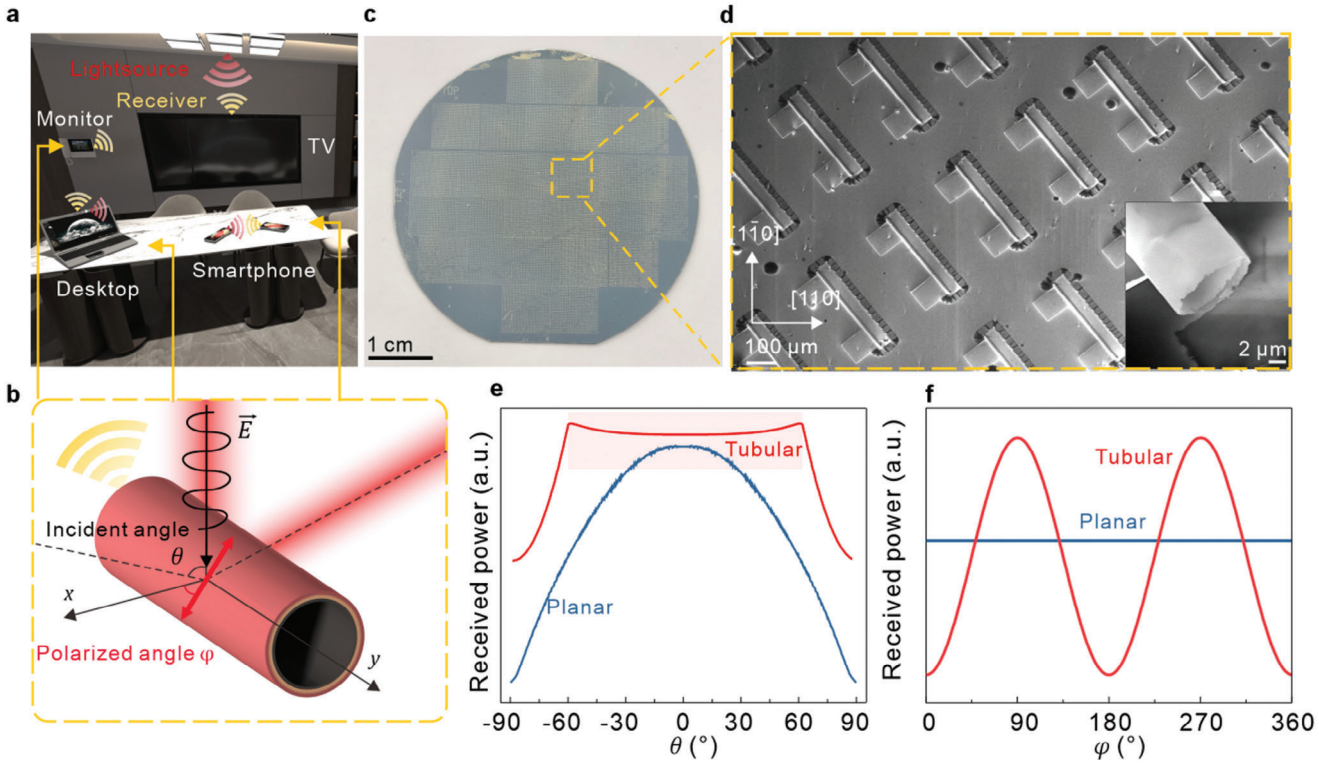

Figure 1. Schematic and morphology characterization of Gr-readout SiGe/Si photodetectors. a) Application scenario diagram of rolled-up Gr-readout SiGe/Si photodetectors. b) Schematic diagram of Gr-readout SiGe/Si microtube photodetector. c) Optical image of SiGe/Si microtube array on a 2-inch wafer. d) SEM image of the Gr-readout SiGe/Si tubes (Inset: channel area of Gr-readout SiGe/Si microtube). e) Simulated absorbed power as a function of incident angle for tubular and planar structures. f) Simulated absorbed power as a function of polarized angle for tubular and planar structures.

incident direction can be achieved (Figure S7, Supporting Information). In addition, the tubular structure decreases the dependence of the channel on the incident angle as in the case of planar devices.[16] The microtube structure can efficiently absorb a wider range of incident light and facilitate multiple reflections, thereby enhancing the utilization efficiency of the incident light (Figure S8, Supporting Information). Therefore, the out-of-plane structure is responsive to a wider range of incident angles, providing a wider FOV (Figure 1e). Moreover, the structural anisotropy of the microtube has local effects on polarized light, enabling the realization of an on-chip polarization detector (Figure 1f). Therefore, we integrate this structure with a 2D photoelectric readout system to produce a photodetector with high performance, offering a cheap and high-speed design scheme for wide-angle, encrypted, and high-speed VLC.

The crystal quality and strain of nanomembranes are vital for the fabrication and performance of photodetectors. The grain boundaries and strain-induced dislocations can have a significantly adverse impact on the transport of charge carriers.[17] To solve this problem, we use epitaxial SiGe/Si nanomembranes as a response layer for self-rolled microtubes (**Figure 2a**). At the same time, the chromium (Cr) nanomembrane in this device functions as an electrode, stress layer, and bonding material layer. The Cr electrode, in conjunction with the Gr/SiGe/Si channel, can rapidly collect photogenerated carriers, meeting the requirements for VLC communication. Additionally, the temperature difference during Cr deposition and the difference in thermal expansion coefficients can serve as a stress layer to regulate the diameter of the microtube.[18] Furthermore, the Cr layer on the unrolled substrate portion acts as an output interface, allowing bonding with probes or metal wires, thereby enabling signal readout and performance testing of the device. The layers in the microtube are made of carbon protective layer/Al_2O_3 protective layer/Si layer/$Si_{0.4}Ge_{0.6}$ layer/Cr layer/Al_2O_3 protective layer/Cr protective layer. As shown in Figure 2a, the nanomembrane bends due to the release of the vertical strain gradient, forming an arch structure with uniform curvature. The cross-section of nanomembrane microtubes was characterized by energy-dispersive X-ray spectroscopy (EDS), as shown in Figure 2b where orange represents Si, yellow represents germanium (Ge), and blue represents Cr. The location of these elements corresponds to the positions of Si, SiGe, and Cr layers in the TEM image, and there is almost no noise signal in the non-corresponding regions, which proves that no obvious diffusion or contamination occurs during epitaxial growth and electron beam deposition, ensuring the quality of the device. We further characterized the crystal quality of the Si/SiGe interface using a high-angle annular dark-field scanning transmission electron microscope (HAADF-STEM). As can be seen from Figure 2c, there is a clear contrast at the Si/SiGe interface, while the atomic-scale image further shows that the interface transition region is only ≈2 nm, which is negligible compared to the thickness of Si and SiGe. Moreover, the lattice of SiGe and Si layers are in a completely ordered arrangement,

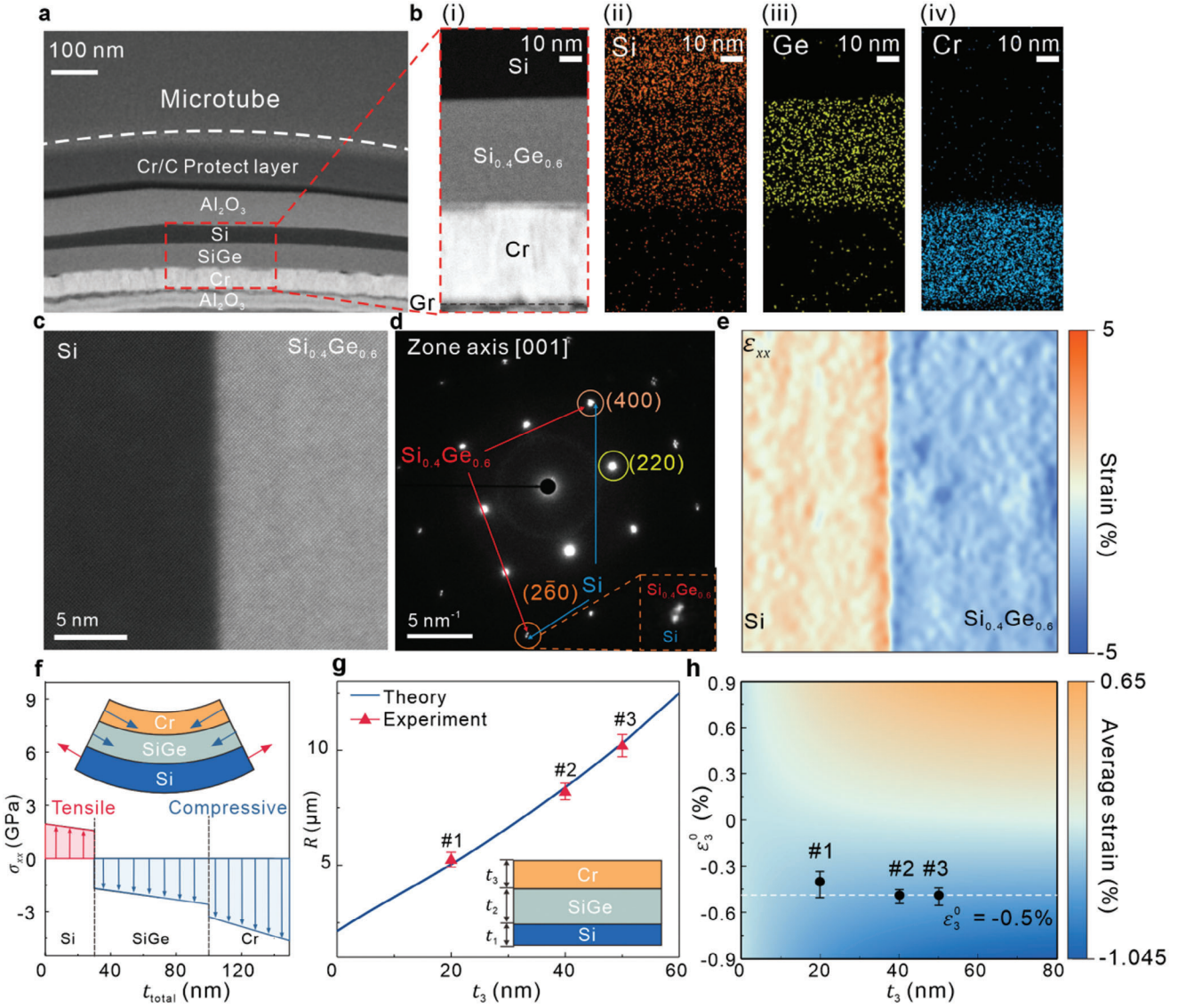

Figure 2. Structural characterization of microtube photodetectors. a) Cross-sectional TEM image of rolled-up Gr/SiGe/Si microtube. b) i) Enlarged TEM image of rolled-up Gr/SiGe/Si microtube. EDS mappings of ii) Si, iii) Ge, and iv) Cr contents in rolled-up Gr/SiGe/Si microtube. c) Atomic-resolution HAADF-STEM image at SiGe/Si interface in rolled-up SiGe/Si nanomembrane. d) SAED image of SiGe/Si interface. e) Geometric phase image of the in-plane strain of Si and SiGe layers. f) Schematic diagram and calculation of stress distribution in Cr/SiGe/Si multilayer. g) Theoretical calculations and experimental results of curvature radii as functions of Cr layer thickness in Cr/SiGe/Si multilayer. The error bars stand for standard deviation. h) Average strain as a function of initial strain and Cr layer thickness.

thus ensuring good crystal quality and strain gradient in the thickness direction (Figure S9a–d, Supporting Information). At the same time, selected area electron diffraction (SAED) analysis was performed at the Si/SiGe interface, as shown in Figure 2d. The SAED diagram exhibits a clear diffraction pattern and no diffraction ring, which proves that the epitaxial Si/SiGe nanomembrane is a single crystal with good quality and the zone axis is [001]. At the (400) and (2$\bar{6}$0) directions, the diffraction pattern is composed of two diffraction spots. The two points near the diffraction origin (d_{400} = 1.391 Å, $d_{2\bar{6}0}$ = 0.868 Å) are SiGe diffraction spots with larger lattice constant and crystal plane spacing. While the two points far from the diffraction origin in the pattern correspond to the diffraction points of Si (d_{400} = 1.358 Å, $d_{2\bar{6}0}$ = 0.851 Å), which have a smaller lattice constant and crystal plane spacing. Geometrical phase analysis (GPA) can further use the atomic displacement field to perform differential operations to analyze the strain of the TEM atomic resolution image.[19] We calculate the strain of Si and SiGe parallel to the thickness direction, and epitaxial Si and SiGe layers show different strain distributions. When the strain at the interface is set as 0%, we can see that there is a clear and uniform strain evolution, where Si is subjected to the tensile strain of ≈1% due to lattice mismatch. The lattice of SiGe is larger and subjected to ≈−1% compressive strain due to the intermediate Ge composition, indicating that ≈a 2% strain gradient is generated between the two layers (Figure 2e). For the unreleased

Si/SiGe bilayer nanomembrane, the ideal initial strain gradient is $\Delta\varepsilon = \frac{a_{SiGe}-a_{Si}}{a_{Si}} = \frac{(0.4)\times 5.431\text{Å} + (0.6)\times 5.658\text{Å} - 5.431\text{Å}}{5.431\text{Å}} \approx 2.51\%$. When the nanomembrane is released and rolled up, the tensile strain of the Si layer will decrease to realize a stable state with minimal elastic energy, and therefore it exhibits relative stretching compared to the initial state.[20] The planar SiGe/Si interface exhibits a larger strain gradient, which also proves the minimum strain energy theory (Figure S9e–l, Supporting Information). After the releasing process, the compressive strain of the SiGe layer will also decrease, but still keep a compressed state, which will eventually lead to the rolling up of the nanomembrane: the Si layer is the outside of the bending arch, while the SiGe layer is the inside of the bending arch. Compared with the SiGe/Si layer, the Cr layer exhibits relatively low strain but still contributes to the compressive strain in the system. The theoretical analysis of bending is highly consistent with the tubular structures observed in the experiment. We evaluated the SiGe/Si sample with different Cr thicknesses with the force–moment balance that is:

$$\gamma_i = \sum_{i=1}^{n} t_i \tag{1}$$

$$c = \frac{\sum_{i=1}^{n} E_i t_i \varepsilon_i^0}{\sum_{i=1}^{n} E_i t_i}$$

$$t_b = \frac{\sum_{i=1}^{n} E_i t_i \left(\gamma_i + \gamma_{i-1}\right)}{2\sum_{i=1}^{n} E_i t_i} \tag{2}$$

$$\frac{1}{R} = \frac{3\sum_{i=1}^{n} E_i t_i \left(\gamma_i + \gamma_{i-1} - 2t_b\right)\left(c - \varepsilon_i^0\right)}{2\sum_{i=1}^{n} E_i t_i \left[\gamma_i^2 + \gamma_i\gamma_{i-1} + \gamma_{i-1}^2 - 3t_b\left(\gamma_i + \gamma_{i-1} - t_b\right)\right]} \tag{3}$$

where E_i is the Young's modulus, t_i is the thickness of nanomembrane, and ε_i^0 is the initial strain difference between two adjacent layers, and $i = 1, 2, 3$ is the layer number of nanomembrane, which represents Si, SiGe, and Cr layer respectively. The initial strain of Si and SiGe layer are set as 1.25% and −1.25% representatively to meet the strain gradient at the epitaxial interface in ideal $Si_{0.4}Ge_{0.6}$/Si NM. Due to the ultrathin thickness of Gr, the force and moment of Gr is neglected to simplify the model. In Cr/SiGe/Si multilayer system, the stress can be calculated as:

$$\sigma_{xx} = E\left(c + \frac{t_{total} - t_b}{R} + \varepsilon^0\right) \tag{4}$$

As shown in Figure 2f, the stress distribution of each layer is related to its thickness and initial strain, exhibiting two obvious regions, that is, tensile stress in Si and compressive stress in SiGe/Cr, which is consistent with the strain distribution in GPA. When taking ε_i^0 as −0.5%, we can see that the theoretical calculation and experiment results are in good consistency (Figure 2f). In the samples #1–3 with different Cr thicknesses t_3 is 20/40/50 nm, R is determined to be 5.24 ± 0.318 µm/8.20 ± 0.362 µm/10.21 ± 0.486 µm, respectively (Figures S10,S11, Note S2, Supporting Information). Utilizing the equation, we can evaluate the initial strain in the Cr layer is ε_i^0 = −0.38–−0.53% within the standard deviation of sample #1–3. Due to the compressive strain in the adjacent SiGe and Cr layers, the average strains of the rolled-up microtubes still exhibit compressive strain in the ranges of −0.3%–−0.6%, which will help to affect the band structure of Gr/SiGe heterostructure and Dirac point of Gr (Figure 2g).

Based on the rolled-up microtube structure, the assembly of the Gr-readout layer will further enhance the performance of photodetectors in terms of material and structural design. Due to the detachment of the microtube structure from the substrate and the processing steps during microtube fabrication, the microtube detector exhibits a lower dark current compared to planar detectors (**Figure 3a**). At the material structure level, in planar devices without microtube processing, the ultrathin thickness of 2D materials makes their physical properties highly susceptible to the substrate and environmental influences, resulting in significant scattering and the formation of impurity centers.[21] Additionally, compared to the high-quality SiGe/Si epitaxial interface, the disorder, roughness, and potential impurities at the SiO_2/Si interface further affect the carrier transport in the nanomembrane.[22] The sacrificial layer release process using hydrofluoric acid can effectively dissolve and remove the oxide layers of SiGe and Si, reducing carrier recombination centers,[23] while passivating the surface dangling bonds with Si—H and Ge—H bonds, thereby lowering the probability of non-radiative carrier recombination.[24] Acetone further cleans the surface, particularly reducing the impact of potential organic residue on Gr performance.[25] At the same time, the introduction of Gr will significantly improve the conductivity and resistance to electrical/thermal breakdown in photodetectors due to its excellent electrical and thermal conductivity and build a good contact interface for microtubes. As shown in the inset of Figure 3a, the Gr/Si/SiGe device exhibits a linear current relationship over the voltage range of −10 to 10 V, demonstrating excellent ohmic contact in the microtube device. For the planar Gr/SiGe/Si device, there are some fluctuations in the dark current at higher voltages, but overall, it also shows a linear contact behavior. For Si/SiGe microtube photodetectors without transferring Gr, the asymmetry of the microtubes and the residual surface states during rolling will cause instability in the carrier transport characteristics, and when the voltage is increased, the current will exhibit an unstable fluctuation state (Figures S12,S13, Supporting Information). In addition, due to carrier velocity saturation, the current of planar Si/SiGe devices will reach saturation at high voltage,[26] which will significantly affect their current gain and frequency response. In contrast, Gr/Si/SiGe devices with transferred Gr show good contact from −10 to 10 V. Current–voltage characteristics can be more intuitively reflected by its logarithmic coordinates, as shown in Figure 3b. Both types of Gr-coupled photodetectors exhibit linear responses, while the planar Si/SiGe photodetectors exhibit a sudden change in current curvature under high voltage (log (V) = 0.9–1), indicating that the microtube structure has insufficient heat dissipation under excessive voltage, which will lead to electrical breakdown or thermal breakdown (Figure S13, Note S3, Supporting Information). Therefore, Gr improves the electrical and thermal stability of the photodetector at the same time. To analyze the energy band of the Gr/SiGe interface, we prepared Au/Gr/SiGe/Si multilayer structures to determine the work functions of Gr and SiGe. With a more stable work function of the Au layer, we can then acquire a more

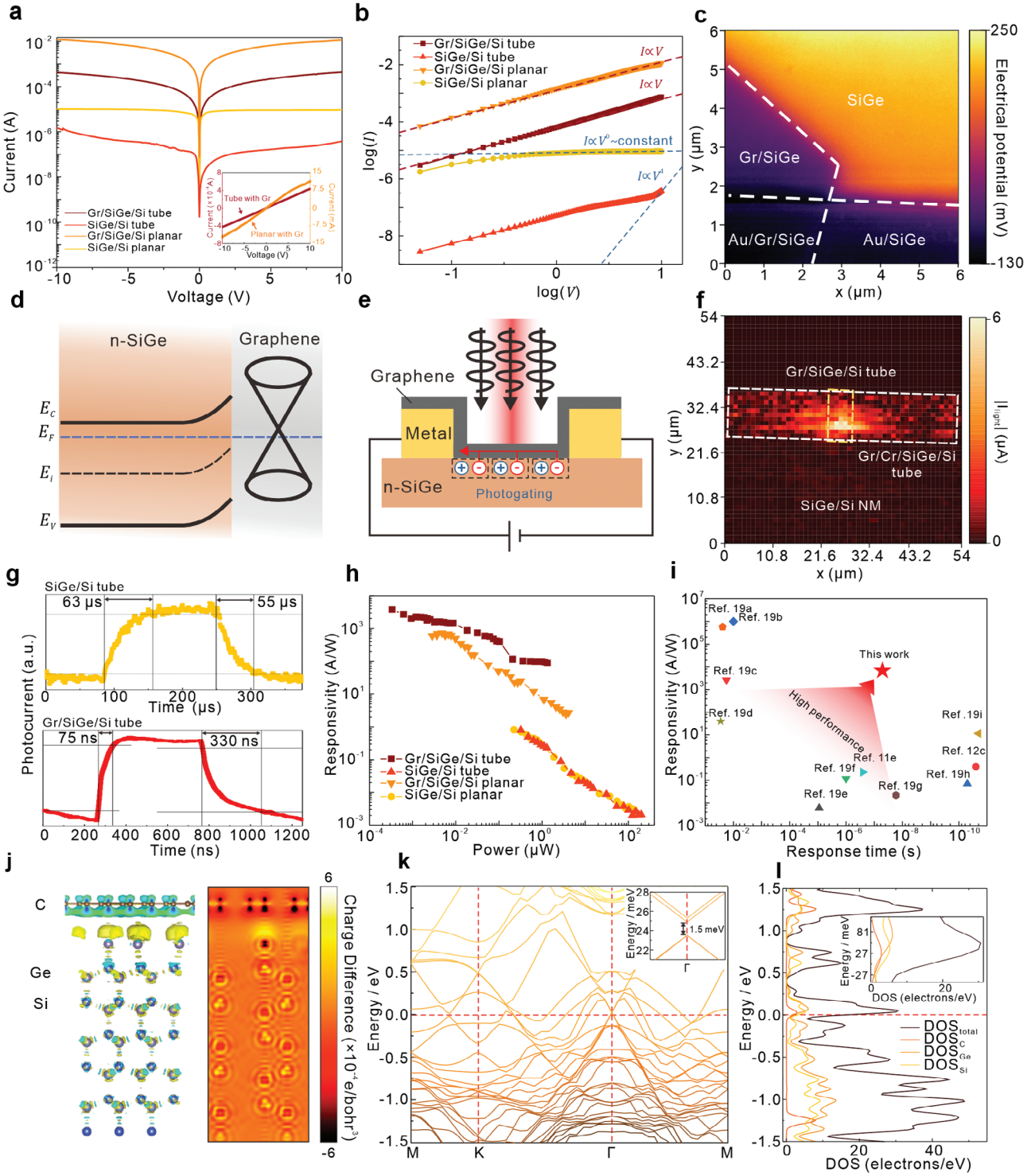

Figure 3. Electrical performance and photodetection mechanism of Gr-readout Si-based tubular photodetectors. a) *I*–*V* curve of photodetector from $V = -10$ to 10 V (Inset: *I*–*V* curve of Gr/SiGe/Si tubular and Gr/SiGe/Si planar photodetectors from $V = -10$ to 10 V in linear scale). b) log(*I*)–log(*V*) curve of photodetectors. c) SKPM mapping of potential distribution in Au/Gr/SiGe multilayer heterostructure. d) Energy band of the interface of Gr/SiGe heterojunction. e) Carrier transport and photogating in Gr/SiGe interface in photodetectors. f) Photocurrent mapping of Gr-readout SiGe/Si microtube photodetector. g) Response time of SiGe/Si photodetector (top yellow line) and Gr-readout SiGe/Si microtube photodetector (bottom red line). h) Relationship between responsivity of photodetectors and light power ($\lambda = 450$ nm). i) Performance comparison between Gr-readout SiGe/Si photodetectors and other 2D material and semiconductor photodetectors. j) Schematic of the simulated structure of Gr/SiGe (111) with its isosurfaces of charge-difference density and the distribution of charge–density difference on the lattice plane (110). k) Simulated energy band of Gr/SiGe (111) (Inset: energy band near the Γ point). l) DOS of C, Si, and Ge in Gr/SiGe (111) (Inset: DOS of Gr/SiGe near the Dirac point of Gr).

accurate result of the work function in Gr and SiGe. As can be seen from Figure 3c, the multilayer exhibits only a maximum potential difference of ≈380 meV, and there is only a potential difference of ≈150–250 meV between Gr/SiGe nanomembrane and SiGe nanomembrane (Figure S14, Supporting Information). Simultaneously, we used Au to calibrate the work function of Gr and SiGe. The work function of Au is typically in the range of 5.0 to 5.1 eV, so we can conclude that the work function of Gr is ≈4.9–5.0 eV, while the work function of SiGe is 4.65–4.75 eV, which is consistent with the value of n-type SiGe. Based on the information from scanning Kelvin probe microscopy (SKPM), we can determine the energy level of the Gr/SiGe interface in microtube photodetectors (Figures S14,S15, Supporting Information). As shown in Figure 3d, since Gr typically adsorbs molecules in air such as oxygen in the atmospheric environment, its Fermi level is below the Dirac point, indicating the characteristics of lightly doped p-type semiconductors.[27] At the interface between n-type SiGe and p-type Gr, the SiGe nanomembrane will slightly reduce the n-type carrier concentration due to the flattening of the Fermi level between SiGe/Gr structures, but due to the small difference in work function, there will be no inversion layer, ensuring low-noise and high-speed transmission of carriers. The band structure at the Gr/SiGe interface is critical to both the contact type and the performance of the device. Modification of Gr can tune its band structure and refine the graphene/semiconductor contact, which has been reported in recent research.[28] One of the most prevalent methods are heteroatom doping methods. Doping Gr with elements adjacent to carbon, such as boron[29] or nitrogen,[30] modifies the projected energy states of carbon atoms and introduces new states from the dopants. This interaction results in a novel density of states (DOS) and an adjusted band structure for the material. These heteroatom doping techniques provide promising methods for tailoring the band structure of Gr, potentially enhancing metal-semiconductor contacts. Previous studies have shown that oxygen adsorption can lower the Fermi level of Gr, causing it to behave as a p-type semiconductor.[27a] This phenomenon can similarly adjust the band structure of Gr. The Gr/SiGe/Si microtubes are also exposed to atmospheric conditions leads to oxygen adsorption. This behavior provides a plausible explanation for our observations of p-type Gr. The reduction in the Fermi level due to oxygen adsorption can also decrease the interface SBH, thereby mitigating the effects of Fermi-level pinning. As shown in Figure 3e, when light is incident on the Gr/SiGe nanomembrane, the photogenerated carriers in SiGe are transported through Gr to the electrode and converted into an electrical signal. In this device, Gr compensates for potential issues of scattering from contamination in the process and defect recombination in the carrier transport process within SiGe, significantly enhancing the transportation process of carriers. Meanwhile, SiGe overcomes the limitations of single-atomic-layer thickness in Gr, such as weak light absorption and easy saturation of photoresponse, achieving complementary properties within the material system. It is also worth noting that the fixed holes in SiGe at the Gr/SiGe interface will generate an additional electric field and realize a photogating effect, which can further increase the carrier concentration and sensitivity to incident light.[31] We also performed photocurrent mapping on Gr/Si/SiGe microtubes. The photoresponse is mainly derived from the Gr/Si/SiGe channel, while the Gr/Cr/Si/SiGe electrode region did not show obvious photocurrent (Figure 3f). It is confirmed that the photodetection mechanism is not Schottky heterojunction, ensuring the stability and low noise characteristics of the device. Gr-readout layer is also important for reducing the response time of microtubes, which is essential for high-frequency detection and high-speed communication. The current–time diagram in Figure 3g shows the rise times and fall times of Si/SiGe microtubes and Gr/Si/SiGe microtubes. Due to the limitation of the SiGe/Si mobility, the Si/SiGe photodetector only shows a rise time of 63 µs and a fall time of 55 µs, and the fastest response frequency can only reach the order of ≈100 kHz, which is difficult to meet the needs of high-speed VLC. The rise time and fall time in Gr/Si/SiGe microtubes are accelerated to 75 and 330 ns respectively, and the responsivity will be improved by $\approx 10^3$ orders of magnitude. Thus, high-speed optical communication on the order of ≈100 MHz can be realized, which can be also observed in planar devices (Figure S16, Supporting Information). It is worth noting that in the Gr/Si/SiGe microtube, the influence of defects and trap states on fall time becomes obvious, which will trap photogenerated carriers and exhibit a relatively slow fall time because of the slow release of trapped holes in photogating effect.[31a] Although the application of Gr can speed up the carrier transport behavior of the interface, it is not entirely able to eliminate the impact. At the same time, we also investigated the relationship between the dark current and the response of the microtube photodetector. When voltage is applied, the dark current exhibits minimal variation over 30 s, with the lowest fluctuation being 2.51% at 1 V. For both strong and weak light incidence, 5 and 1 V can be selected as operating voltages based on the response-to-dark-current ratio. This ensures good device performance while minimizing the adverse thermal effects of current on the device (Figure S17, Supporting Information).

As shown in Figure 3h, The microtube and planar Gr-readout SiGe/Si photodetectors demonstrated responsivities of 6803 and 595 A W^{-1} respectively. Based on a light-trapping structure, fast carrier-transport layer, and high-quality single-crystal nanomembrane, the microtube photodetector exhibits a good combination of responsivity and response time in the 2D material/semiconductor photodetector system (Figure 3i).[11e,12c,32] The rapid transport of the photogenerating carriers in the Gr prevents the scattering from the Si/SiGe layer to the electrodes, and significantly improves the sensitivity of the photodetector, allowing the detection of nW-level incident light. In contrast, the Si/SiGe planar and microtube photodetectors exhibited sensitivities of only 814 and 786 mA W^{-1}, respectively, which are unable to detect weak light. To further analyze the principle of improved performance, the carrier transport and electronic structure in Gr/SiGe (111) microtubes will be discussed. The charge–density difference ($\Delta\rho$) is obtained by Bader-charge analysis[33] with the help of Visualization for Electronic and STructural Analysis.[34] As shown in Figure 3j, the calculated charge–density difference between Gr and SiGe is 0.0012 e $bohr^{-3}$, where Gr performs as the acceptor and SiGe performs as the donator, which is consistent with the results of SKPM mapping in Figure 3c. The energy band structure is shown in Figure 3k. Influenced by SiGe, the Dirac point of Gr is above the Fermi level. Moreover, the valence band and the conduction band are separated by a gap of 1.5 meV at the Dirac point, enhancing the carrier absorbance.[35] The electronic states of C atoms are concentrated near the Dirac

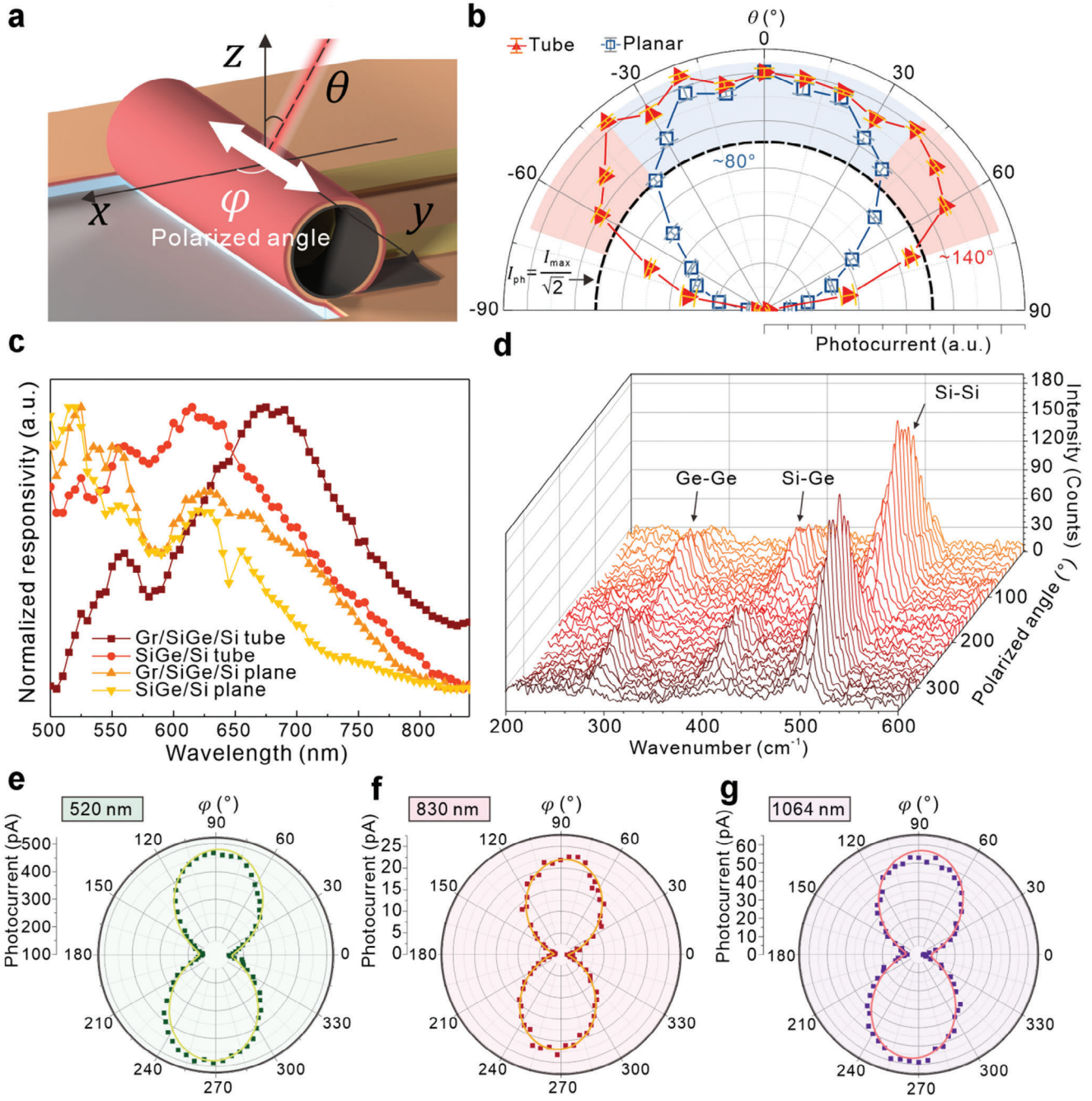

Figure 4. Enhanced multifunctional photodetection of Gr-readout SiGe/Si microtube photodetector. a) Schematic diagram of incident angle and polarized angle of incident light in Gr-readout SiGe/Si microtube photodetectors. b) Omnidirectional photodetection of Gr-readout SiGe/Si microtube photodetectors. The error bars stand for standard deviation. c) Normalized responsivity of photodetectors from 500 to 840 nm (voltage = 1 V, power = 2 μW). d) Angle-resolved polarized Raman spectra of SiGe/Si layer, with Ge–Ge, Si–Ge, and Si–Si peaks marked. Photocurrents under polarized incident lights with wavelengths of e) 520 nm, f) 830 nm, and g) 1064 nm ($V = 0$ V).

point referring to Figure 3l, which means that Gr exhibits high mobility for photodetection.

The combination of structural characteristics and the Gr-readout layer is proven to enhance the capabilities of the photodetector while maintaining its high performance. As shown in **Figure** 4a, the Gr/Si/SiGe microtube photodetector is implemented to achieve wide-angle incident light detection perpendicular to the tube axis, and high-performance polarization detection, perpendicular to the substrate plane. As illustrated in Figure 4b, the photocurrent response of the microtube from $\theta = -70°$ to 70° incident angles results in effective photoresponse ($I_{ph} \geq \frac{I_{max}}{\sqrt{2}}$), with obvious photoresponse achieved in the range

of $\theta = -80°$ to 80°. Meanwhile, the planar photodetector can maintain effective photodetection from only $\theta = -40°$ to 40°, exhibiting smaller receiving angle. This feature is critical for signal reception in complex optical communication applications. When self-rolling occurs, the polarization sensitivity of the thickness direction of Gr can be altered, enabling multi-gain polarization detection with microtubes. As illustrated in Figure 4c, the photodetectors exhibit effective photoresponse in the wavelength range of 500–800 nm, and the tubular structure demonstrating a stronger response in the 600–700 nm region compared to the planar structure. This is due to the ability of the microtube structure to confine incident light within the cavity, leading to an enhancement. In both planar and microtube devices, the incorporation of Gr enhances their response in the long-wave visible band and the near-infrared band. We also conducted corresponding simulations to investigate the photoresponse of four types of devices, which also exhibit obvious photoresponse in the visible spectrum (Figure S18, Supporting Information). The polarized Raman results for the microtube structure show that the vibration peaks of Si—Si bonds, Si—Ge bonds, and Ge—Ge bonds in the SiGe/Si nanomembrane exhibit responses to light of different polarizations, with polarization dichroic ratios of 2.87, 3.11, and 3.60, respectively (Figure S19, Supporting Information). As shown in Figure 4e–g, under incident light of 520, 830, and 1064 nm, the Gr/Si/SiGe microtube photodetector exhibits high dichroic ratios. For 520 nm, the dichroic ratio is $\frac{488.7\text{pA}}{146.5\text{pA}} \approx 3.33$; for 830 nm, the dichroic ratio is $\frac{23.08\text{pA}}{1.43\text{pA}} \approx 16.09$; for 1064 nm, the dichroic ratio is $\frac{60.55\text{pA}}{5.97\text{pA}} \approx 10.13$. In the visible light range, such as at the wavelength of 520 nm, the polarization response mainly originates from the Gr and SiGe/Si semiconductor layers. However, the semiconductor layer has a larger thickness and higher absorption of light with a photocurrent component that is insensitive to polarized light. Therefore, the dichroic ratio is mainly attributed to the spatial anisotropy of the microtube structure, resulting in a dichroic ratio of only $\frac{488.7\text{pA}}{146.5\text{pA}} \approx 3.33$. When the wavelengths are 832 and 1064 nm, the response of the semiconductor nanomembrane to infrared light is significantly reduced, allowing the polarization photoresponse to be dominated by the response of the Gr tubular structure. Benefiting from the polarization sensitivity of Gr and the anisotropy of the microtube structure, the dichroic ratio of the Gr/Si system photodetector based on the 3D tubular structure is higher than that of common 1D polarization-sensitive materials and in-plane anisotropic materials and shows comparable performance to photodetectors with micro-nano structures and external field-control designs (Figure 20, Tables S1–S3, Supporting Information). The performance demonstrated by this device indicates that the material-structure coupling approach will contribute to further advancements in the design of polarization photodetectors. The higher dichroic ratio in the near-infrared band is derived from the relative low responsivity of the SiGe/Si nanomembrane due to the band gap. In this condition, polarization-sensitive detection is mainly contributed by Gr, where its polarization-sensitive photocurrent component accounts for a larger proportion of the photoresponse. Simulations using the finite-difference time-domain (FDTD) method further reveal for suitable wavelength, polarized light will coincide at a focal point, resulting in significant light enhancement in the tube cavity, further improving the polarization detection capability of microtubes. When the incident light wavelength is 830 nm, there is no significant focusing on the tube cavity when the polarization angle $\alpha = 0°$, but when the polarization angle is gradually increased to $\alpha = 45°$ and $\alpha = 90°$. The electromagnetic field in the center of the tube cavity appears to be significantly intensified, thereby further enhancing the photodetection ability of the microtube and achieving the high-photoresponse at 90° polarization (Figure S21, Supporting Information). Simulations of the Gr microtube structure also reveal that there is a significant selection ratio for 90° polarized light and 0° polarized light, which is hard to be realized in planar Gr (Figures S21,S22, Supporting Information). In contrast, the SiGe/Si microtube, which relies solely on structural anisotropy for detection, exhibits a maximum dichroic ratio of only 1.50 (Figure S23, Supporting Information). Theoretical models further disclose the selection effect of the tubular structure and anisotropic dielectric constant of Gr on the absorption of polarized light, confirming the key role of Gr as a polarization-selective material in the device. The microtube can be considered as a semi-infinite ring structure, and the inner Gr layer exhibits an anisotropic optical coefficient and polarization-dependent absorption (Figure S24, Note S4, Supporting Information). Theoretical calculations also explain the higher dichroic ratio of the Gr/Si microtube structure in the infrared region, attributed to the differences in absorption ratios across various wavelengths (Figure S25, Supporting Information). For polarization detection, increasing the device voltage tends to increase the polarization-insensitive photocurrent component, thereby reducing the dichroic ratio. Therefore, performing polarization detection at zero bias maximizes the sensitivity advantage of the microtube device (Figure S26, Supporting Information). Additionally, the microtube detector fabricated on centimeter-scale substrates exhibits good stability. The current–voltage curve shows a maximum current in the range of $I(V) \approx 0.325\text{–}0.575 \times 10^{-4} \times V$ over a voltage range of −5 to 5 V, with the current also exhibiting good linearity. Furthermore, at $V = 1$ V, the device demonstrates a fast and stable photoresponse to 450 nm incident visible light, indicating its potential for large-scale applications (Figure S27, Supporting Information). The microtube structure provides an ideal platform for the large-area interaction between out-plane 2D materials and incident light, which is also promising in the research of the unique out-plane physical properties of few-layer material.

Transmission testing of photodetectors in VLC systems is crucial to verify their feasibility as signal receivers. Thus, we establish a VLC test platform based on laser diode (LD) to characterize the performance of Gr-readout photodetectors (**Figure 5**a, and Experimental Section). Among the performance of VLC receivers, the −3 dB bandwidth plays a key role when transmitting data. As can be seen in Figure 5b, we test the −3 and −10 dB bandwidths of microtube structures, which are 50.5 and 64.9 MHz respectively. The high bandwidth of microtube devices benefits from the high mobility of the Gr layer and the ohmic contact in the Gr/Cr electrode interface. In practical VLC, the bit error rate (BER) relationship depends on both bandwidth and modulation algorithm, and the OOK modulation method can achieve better recognition accuracy for signals with weak signal-to-noise ratio. Furthermore, when the signal-to-noise ratio (SNR) of light is greater than 17.5 dB, the devices can also exhibit

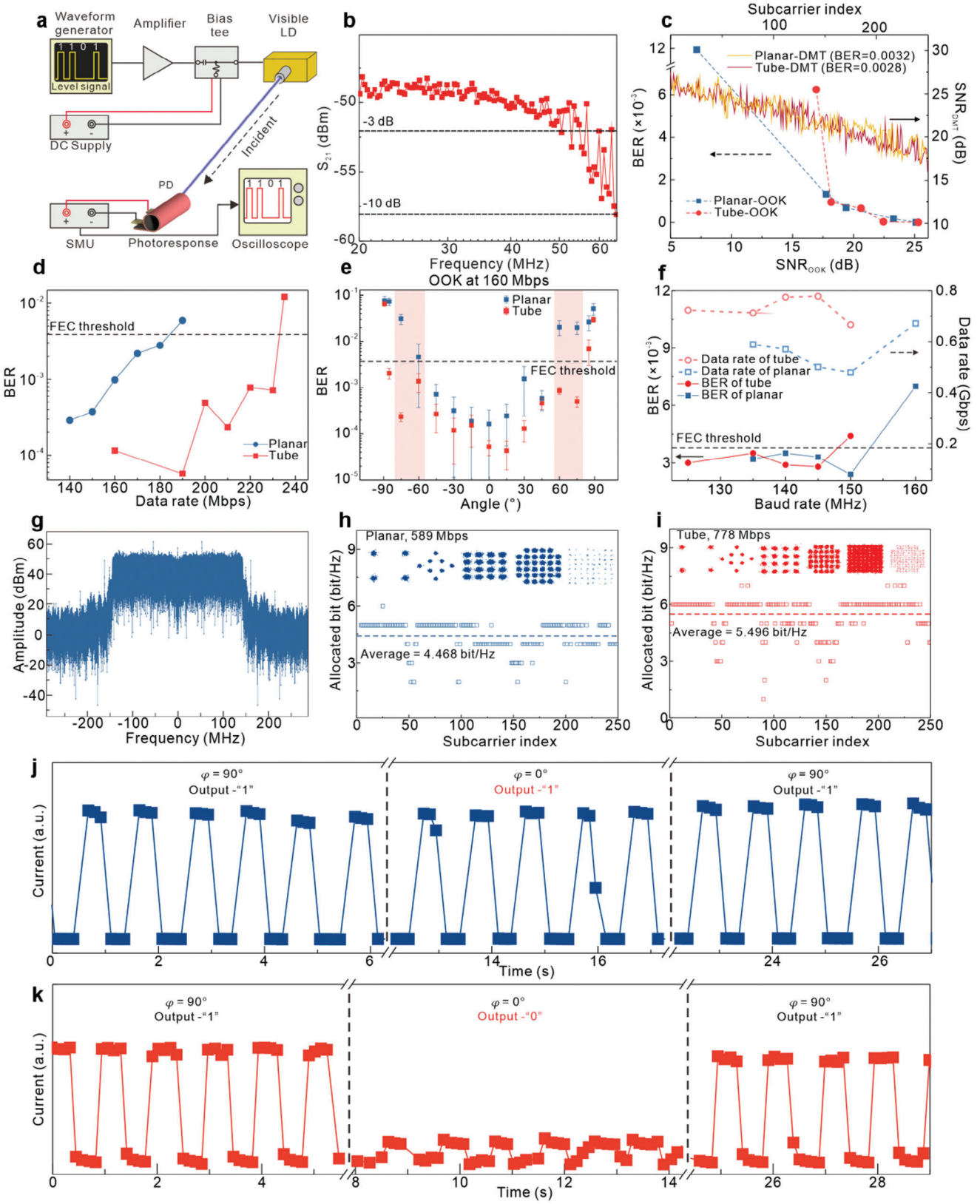

an effective response, proving the applicability of the device in the OOK modulation method. As for the communication system using the adaptive DMT modulation technique, we are using a bit-loading algorithm. The objective is to make full use of the SNR to increase the spectral efficiency toward the high data transmission rate.[36] For the planar structure, the device exhibits an SNR ranging from 16.9 to 27.1 dB at a BER of 0.0032, while the microtube structure shows an SNR ranging from 15.9 to 27.5 dB at a BER of 0.0028. Both structures can be effectively applied in VLC systems while fully utilizing the available bandwidth (Figure 5c; Figure S28, Supporting Information). In the OOK modulation method, the planar device can achieve the fastest data rate of 180 Mbps at the forward error correction bit rate threshold, while the microtube structure can reach up to 230 Mbps at this threshold, which is ≈30% faster than the planar device (Figure 5d). We also characterized the directional incident light VLC of the planar and the microtube devices. At a data rate of 160 Mbps, we tested the device with OOK modulation at different angles. A significant advantage of microtube devices is the on-chip wide-FOV photodetection for high-speed VLC. It can be seen in Figure 5e that the planar device can only achieve VLC with acceptable BER in the range from $\theta = -45°$ to 45°, while microtube structures can receive a wider incident signal from $\theta = -75°$ to 75°, meeting the requirement of wide-FOV. Based on the high spectral efficiency advantage of DMT modulation, we can enable the device to achieve sub-Gbps communication rates. Specifically, in DMT modulation, planar devices, and tubular devices can reach data rates of 589 and 778 Mbps at the baud rate of 135 and 145 MHz respectively (Figure 5f). A high SNR is essential for reliable signal transmission. The power spectrum of the microtube photodetector indicates that there is some minor loss in the high-frequency region due to the bandwidth limitation of 145 MHz (Figure 5g), which remains below the threshold. It is worth noting that the loss can be also observed in planar devices with the bandwidth limitation of 135 MHz (Figure 5f; Figures S29,S30, Supporting Information). The constellation diagram intuitively demonstrates the communication quality. In planar devices, DMT can achieve a maximum of 64-QAM modulation with an average order of 4.468 (Figure 5h), whereas in microtube devices, it can reach up to 128-QAM modulation with an average order of 5.496 (Figure 5i). Therefore, the tubular photodetector enables higher data transmission rates under similar baud rate conditions. By utilizing the polarization sensitivity of the Gr layer and microtube structure, the Gr/Si/SiGe microtube photodetector can successfully process the encrypted polarization signal. As illustrated in Figure 5j, when polarized light signals with $\varphi = -0°$, and 90° are detected by the planar photodetector, the SiGe/Si layer does not exhibit a spatially anisotropic structure, and the Gr layer demonstrates no significant polarization response in the in-plane state.[37] Therefore, when the polarization angle is altered from 0° to 90°, the current response of the planar photodetector does not change significantly, and the interpreted signal remains a constant on-state "1" signal. On the other hand, Figure 5k illustrates that the photoresponse of the microtube photodetector will significantly reduce the polarization angle response at 90°, thus interpreting the off-state "0" signal. This demonstrates that besides the interpretation of light intensity in optical communication, the information contained by polarized light can be further analyzed, thereby enhancing the dimension of information transmission and providing a class of methods for high-throughput encrypted optical information reception.

3. Conclusion

In conclusion, we propose a Gr-readout SiGe/Si nanomembrane self-rolled microtube photodetector for chip-level wide-FOV, high-speed VLC, and polarization-sensitive encrypted VLC applications. The microtubes prepared by the self-rolled technique maintain the crystal structure of SiGe/Si nanomembranes and enable damage-free preparation of the semiconductor nanomembrane 3D structures. The Gr-readout layer and microtube structure exhibit excellent electrical stability and response time, resulting in significant improvements in visible photodetection sensitivity. The SKPM measurement and simulation revealed the low energy-barrier contact, carrier transport mechanism at the Gr/SiGe interface, and the opening of the Gr Dirac point will further enhance carrier transport efficiency. The photodetector enables omnidirectional detection of incident light, and the thickness direction of the Gr layer in the tube cavity can be coupled with polarized light, to realize high dichroism polarization photodetection. Notably, the Gr/SiGe/Si microtube structure provides significant advantages in data rate, FOV, and polarization detection in VLC compared to planar devices, without the need to incorporate additional optical components. The proposed microtube photodetectors will provide an innovative solution for the design of a wide detection angle, multi-function, miniaturized on-chip light receiver, and has great application potential in the fields of portable devices, internet of things, high-efficiency VLC, and information security.

4. Experimental Section

Fabrication of Gr-Readout SiGe/Si Photodetectors: The Si/SiGe were grown by molecular beam epitaxy on a 4-inch Si wafer and then bonded on a 300 nm SiO_2/500 µm Si wafer. Photoresist S1813 was spin-coated at 3000 rpm for 30 s, and electrode patterns were defined by the direct laser writing system. After development, the Cr electrode layer was deposited

Figure 5. VLC performance of microtube Gr-readout SiGe/Si photodetectors. a) Schematic diagram of photodetection test setup. b) −3 and −10 dB bandwidth of Gr-readout SiGe/Si microtube photodetectors. c) BER and SNR of incident light of Gr-readout SiGe/Si photodetectors in OOK modulation and DMT modulation. d) Relationship between BER and data rate of Gr-readout SiGe/Si planar and microtube photodetectors in OOK modulation. e) Omnidirectional OOK modulation of Gr/SiGe/Si planar and microtube photodetectors when data rate = 160 Mbps. The error bars stand for the standard error of the mean. f) Relationship between BER, data rate, and baud rate of Gr-readout SiGe/Si planar and microtube photodetectors in DMT modulation. g) Power spectrum of rolled-up Gr/SiGe/Si photodetectors. h) Allocated bit distribution of DMT signals of planar photodetector at a data rate of 589 Mbps (Inset: constellation diagrams of the received signals with the loaded bit number from 2 to 6 bits symbol^{-1}). i) Allocated bit distribution of DMT signals of tubular photodetector at a data rate of 778 Mbps (Inset: constellation diagrams of the received signals with the loaded bit number from 2 to 7 bits symbol^{-1}). Current signal of polarized VLC in Gr-readout SiGe/Si j) planar photodetectors and k) tubular photodetectors.

by e-beam evaporation at 1 Å s^{-1}. The etching window of the Si/Ge layer was then exposed and etched by reactive ion etching in the condition of 18 sccm CHF_3 flow rate, 35 sccm SF_6 flow rate, 30 mT chamber pressure with 50 W power.[38] After e-beam evaporation and reactive ion etching, the S1813 photoresist was removed in acetone with ultrasonic cleaner for 120 s. The Gr on copper foil was a commercial product from PrMat. Before wet transfer, poly (methyl methacrylate) (PMMA) A7 was spin-coated on Gr at 1500 rpm for 30 s, and then heated on a hot plate at 180 °C for 30 min. Then, the PMMA/Gr/copper foil would be immersed in copper etchant ($HCl:H_2O:H_2O_2$ = 10:20:3.75) for 10 min to release PMMA/Gr from the copper foil. The released PMMA/Gr was cleaned by deionized water rinsing for 3 times and transferred onto SiGe/Si patterns with Cr electrodes. The transferred Gr/Si/SiGe chips were heated on a hot plate at 180 °C for 30 min and then cleaned in acetone at 80 °C for 60 min to remove PMMA. Another lithography was applied to define the Gr photodetection area. The Gr/SiGe/Si samples were immersed in 40% HF solution for 40 min to release the Gr/SiGe/Si layer from the SiO_2 sacrificial layer. After release, the Gr/SiGe/Si samples were sent to a critical point drying with acetone to prevent structural collapse caused by surface tension.

Characterization of Nanomembrane and Photodetectors: Morphological characteristics of the Gr/SiGe/Si nanomembrane and tubular photodetectors were performed via SEM Zeiss Sigma 300. TEM, STEM, EDS characterization, and FFT analysis of the SiGe/Si/SiO_2 layer was performed by JEOL ARM200F. Raman spectra of Gr/SiGe/Si nanomembrane were performed by Renishaw inVia. The optoelectrical properties of Gr-readout SiGe/Si photodetectors were performed by Keysight B2902B at room temperature. Keysight 33500B waveform generator, Stanford Research Systems Model SR830 DSP lock-in amplifier, and Stanford Research Systems Model SR570 low-noise current preamplifier were utilized to extract photocurrent signals from current signals. Polarized photodetection was performed by Metatest MStarter 200.

Calculation of Charge–Density Difference and Electronic Structure: All simulation works were carried out based on density functional theory (DFT) through the first-principle calculations using the Vienna ab initio simulation package (VASP) code,[39] where projected-augmented-wave potentials[40] were selected and the generalized gradient approximation parametrized by Perdew–Burke–Ernzerhof[41] was employed for the exchange and correlation functional. The VASPKIT[42] was induced in support of the construction of a simulation model. The plane-wave cut-off energy was set as 400 eV, and the first Brillouin zone (BZ) was sampled with a grid of 4 × 4 × 1 ***k*** points. A vacuum layer with a width of 10 Å was used to reduce the effect of adjacent Gr/SiGe (111) slabs. The lattice parameter of SiGe was set as 5.27 Å. The top three rows of SiGe atoms and all C atoms were unfixed during the lattice relaxation. The DFT-optimized Gr lattice parameter was 2.52 Å (Figure S31, Supporting Information). The charge–density difference ($\Delta\rho$) was calculated by:

$$\Delta\rho = \Delta\rho_{Gr/SiGe} - \Delta\rho_{Gr} - \Delta\rho_{SiGe} \quad (5)$$

where $\Delta\rho_{Gr/SiGe}$, $\Delta\rho_{Gr}$ and $\Delta\rho_{SiGe}$ refer to the total charge density of Gr/SiGe, the pristine Gr and SiGe, respectively.

Finite Element Modeling of Electric Field Distribution: The simulation of the electrical field was realized by the FDTD method via Ansys Lumerical 2020. The model consisted of a 30 nm Si/40 nm SiGe/10 µm SiO_2 substrate, and a 30 nm Si/40 nm SiGe/1 nm Gr microtube, where the outer radius of the Si layer was 5 µm because the measurement of photodetection performance and VLC application was based on sample #1. For samples #2 and #3, the corresponding microtube structures had diameters of 8.2 and 10.2 µm, respectively, both of which similarly exhibited sensitivity to linearly polarized light (Figure S32, Supporting Information). The boundary condition along the thickness direction was a perfect match layer, and the boundary condition parallel to the thickness direction was period.

Setup of VLC: The LD was driven by a three-way biasing device, which combined the DC power supply with the signal sequence generated in the signal generator to achieve the emission of the optical signal of the specified modulation method. At this time, an optical detector driven by another DC power supply detected the optical signal emitted by the LD and transmits the generated signal to the oscilloscope. The communication distance between the LD and the optical detector was 0.2 m, and the angle was rotated with the detector as the center of the circle during the angle test (Figure S33, Supporting Information).

Statistical Analysis: The normalization in Figure 4b was performed by scaling the data from the minimum to maximum values into a range of 0 to 1. In Figure 2g, the statistical analysis was conducted with a sample size of $n = 30$ (sample #1), 31 (sample #2), and 30 (sample #3). In Figure 4b, the statistical analysis was conducted with a sample size of $n = 7$. In Figure 5e, the statistical analysis was conducted with a sample size of $n = 6$.

Supporting Information

Supporting Information is available from the Wiley Online Library or from the author.

Acknowledgements

Z.Z., T.C., and Z.L. contributed equally to this work. This work was supported by the National Key Technologies R&D Program of China (No. 2021YFA0715302), the National Natural Science Foundation of China (Nos. 61975035, 62375054, 523B2107, and 623B1003), the Science and Technology Commission of Shanghai Municipality (Nos. 21142200200 and 22ZR1405000), and National Postdoctoral Program for Innovative Talents (Nos. BX20240394). Part of the experimental work was carried out in the Fudan Nanofabrication Laboratory. Part of the computations in this research were performed using the CFFF platform of Fudan University.

Conflict of Interest

The authors declare no conflict of interest.

Data Availability Statement

The data that support the findings of this study are available in the supplementary material of this article.

Keywords

graphene-semiconductor heterostructure, microtube photodetectors, polarization photodetection, visible light communication, wide field of view

Received: September 12, 2024
Revised: October 21, 2024
Published online: November 21, 2024

[1] a) J. Hu, Z. Guo, J. Shi, X. Jiang, Q. Chen, H. Chen, Z. He, Q. Song, S. Xiao, S. Yu, N. Chi, C. Shen, *Nat. Commun.* **2024**, *15*, 2944; b) Y. Zhou, X. Zhu, F. Hu, J. Shi, F. Wang, P. Zou, J. Liu, F. Jiang, N. Chi, *Photonics Res.* **2019**, *7*, 1019; c) J. Wang, C. Chen, B. Deng, Z. Wang, M. Liu, H. Y. Fu, *Opt. Express* **2023**, *31*, 16812.

[2] a) T. Uday, A. Kumar, L. Natarajan, *IEEE Wireless Commun. Lett.* **2021**, *10*, 609; b) X. Zhou, J. Shi, N. Chi, C. Shen, Z. Li, *Opt. Express* **2023**, *31*, 25359; c) V. K. Papanikolaou, P. D. Diamantoulakis, P. C. Sofotasios, S. Muhaidat, G. K. Karagiannidis, *IEEE Trans. Cognit. Commun. Networking* **2020**, *6*, 352.

[3] a) Y. Hou, Z. Wang, Z. Li, J. Hu, C. Ma, X. Wang, L. Xia, G. Liu, J. Shi, Z. Li, J. Zhang, N. Chi, C. Shen, *Sensors* **2024**, *13*, 386; b) B. A. Vijayalakshmi, P. Gandhimathi, M. Nesasudha, *J. Opt.* **2024**, *53*, 933; c) S. Caputo, L. Mucchi, M. A. Umair, M. Meucci, M. Seminara, J. Catani, *Sensors* **2022**, *22*, 8618.

[4] a) Z. Wang, F. Chen, W. Qiu, S. Chen, D. Ren, *Opt. Commun.* **2018**, *410*, 94; b) Z. Wang, Z. Wang, S. Chen, *Opt. Commun.* **2019**, *431*, 229.
[5] a) R. Liu, J. Zhang, H. Zhou, Z. Song, Z. Song, C. R. Grice, D. Wu, L. Shen, H. Wang, *Adv. Opt. Mater.* **2020**, *8*, 1901735; b) B. Huang, J. Liu, Z. Han, Y. Gu, D. Yu, X. Xu, Y. Zou, *ACS Appl. Mater. Interfaces* **2020**, *12*, 48765; c) J. Shi, Z. Xu, W. Niu, D. Li, X. Wu, Z. Li, J. Zhang, C. Shen, G. Wang, X. Wang, J. Zhang, F. Jiang, S. Yu, N. Chi, *Photonics Res.* **2022**, *10*, 2394; d) B. Ouyang, H. Zhao, Z. L. Wang, Y. Yang, *Nano Energy* **2020**, *68*, 104312.
[6] a) R. K. Pal, S. P. Dash, S. Aïssa, D. Ghose, *IEEE Wireless Commun. Lett.* **2024**, *13*, 34; b) P. Nabavi, M. Yuksel, *J. Lightwave Technol.* **2020**, *38*, 4187; c) W. Ali, P. P. Manousiadis, D. C. O. Brien, G. A. Turnbull, I. D. W. Samuel, S. Collins, *J. Lightwave Technol.* **2022**, *40*, 5369; d) D. Milovančev, T. Jukić, N. Vokić, P. Brandl, B. Steindl, H. Zimmermann, *IEEE Photonics J.* **2021**, *13*, 7900513.
[7] a) F. Hu, S. Chen, Y. Zhang, G. Li, P. Zou, J. Zhang, C. Shen, X. Zhang, J. Hu, J. Zhang, Z. He, S. Yu, F. Jiang, N. Chi, *PhotoniX* **2021**, *2*, 16; b) J. Chai, L. Chen, B. Cao, D. Kong, S. Chen, T. Lin, W. Wang, Y. Liu, G. Li, *Opt. Express* **2022**, *30*, 3903.
[8] a) A. Rawat, A. Ahamed, C. Bartolo-Perez, A. S. Mayet, L. N. McPhillips, M. S. Islam, *ACS Photonics* **2023**, *10*, 1416; b) L. Zhang, R. Jiang, X. Tang, Z. Chen, J. Chen, H. Wang, *IEEE Photonics J.* **2022**, *14*, 1.
[9] J. He, B. Zhou, *Opt. Express* **2021**, *29*, 27278.
[10] a) J. A. Rogers, M. G. Lagally, R. G. Nuzzo, *Nature* **2011**, *477*, 45; b) S. Kim, J. Wu, A. Carlson, S. H. Jin, A. Kovalsky, P. Glass, Z. Liu, N. Ahmed, S. L. Elgan, W. Chen, P. M. Ferreira, M. Sitti, Y. Huang, J. A. Rogers, *Proc. Natl. Acad. Sci. USA* **2010**, *107*, 17095; c) H. J. Yang, D. Y. Zhao, S. Chuwongin, J. H. Seo, W. Q. Yang, Y. C. Shuai, J. Berggren, M. Hammar, Z. Q. Ma, W. D. Zhou, *Nat. Photonics* **2012**, *6*, 615.
[11] a) Z. Zhang, B. Wu, Y. Wang, T. Cai, M. Ma, C. You, C. Liu, G. Jiang, Y. Hu, X. Li, X.-Z. Chen, E. Song, J. Cui, G. Huang, S. Kiravittaya, Y. Mei, *Nat. Commun.* **2024**, *15*, 3066; b) B. Xu, X. Lin, Y. Mei, *Cell Rep. Phys. Sci.* **2020**, *1*, 100244; c) Z. Tian, B. Xu, G. Wan, X. Han, Z. Di, Z. Chen, Y. Mei, *Nat. Commun.* **2021**, *12*, 509; d) W. Huang, S. Koric, X. Yu, K. J. Hsia, X. Li, *Nano Lett.* **2014**, *14*, 6293; e) T. Deng, Z. Zhang, Y. Liu, Y. Wang, F. Su, S. Li, Y. Zhang, H. Li, H. Chen, Z. Zhao, Y. Li, Z. Liu, *Nano Lett.* **2019**, *19*, 1494.
[12] a) B. Wu, Z. Zhang, Z. Zheng, T. Cai, C. You, C. Liu, X. Li, Y. Wang, J. Wang, H. Li, E. Song, J. Cui, G. Huang, Y. Mei, *Adv. Mater.* **2023**, *35*, 2306715; b) X. Zhou, Z. Tian, H. J. Kim, Y. Wang, B. Xu, R. Pan, Y. J. Chang, Z. Di, P. Zhou, Y. Mei, *Small* **2019**, *15*, e1902528; c) S. Zhang, F. Gao, W. Feng, H. Yang, Y. Hu, J. Zhang, H. Xiao, Z. Li, P. Hu, *Nanotechnology* **2021**, *33*, 105301; d) B. Wu, Z. Zhang, C. Wang, E. Song, J. Cui, G. Huang, P. Zhou, Z. Di, Y. Mei, *Appl. Phys. Lett.* **2022**, *121*, 060503; e) J. Xu, Q. Wang, M. Shen, Y. Yang, H. Liu, X. Yuan, Y. Zhang, K. Liu, S. Cai, Y. Huang, X. Ren, *ACS Nano* **2024**, *18*, 14978.
[13] B. Wu, Z. Zhang, B. Chen, Z. Zheng, C. You, C. Liu, X. Li, J. Wang, Y. Wang, E. Song, J. Cui, Z. An, G. Huang, Y. Mei, *Sci. Adv.* **2023**, *9*, eadi7805.
[14] a) L. H. Wong, C. C. Wong, J. P. Liu, D. K. Sohn, L. Chan, L. C. Hsia, H. Zang, Z. H. Ni, Z. X. Shen, *Jpn. J. Appl. Phys.* **2005**, *44*, 7922; b) Q. Guo, M. Zhang, Z. Xue, J. Zhang, G. Wang, D. Chen, Z. Mu, G. Huang, Y. Mei, Z. Di, X. Wang, *AIP Adv.* **2015**, *5*, 037115; c) S. Nakashima, T. Mitani, M. Ninomiya, K. Matsumoto, *J. Appl. Phys.* **2006**, *99*, 053512; d) D. Rouchon, M. Mermoux, F. Bertin, J. Hartmann, *J. Cryst. Growth* **2014**, *392*, 66.
[15] a) A. K. Katiyar, B. J. Kim, G. Lee, Y. Kim, J. S. Kim, J. M. Kim, S. Nam, J. Lee, H. Kim, J. H. Ahn, *Sci. Adv.* **2024**, *10*, eadg7200; b) T. G. Mayerhöfer, S. Pahlow, J. J. C. Popp, **2020**, *21*, 2029.
[16] C. Xu, R. Pan, Q. Guo, X. Wu, G. Li, G. Huang, Z. An, X. Li, Y. Mei, *Adv. Opt. Mater.* **2019**, *7*, 1900823.
[17] a) D. Dumin, P. Robinson, *J. Appl. Phys.* **1968**, *39*, 2759; b) Y. Morimoto, Y. Jinno, K. Hirai, H. Ogata, T. Yamada, K. Yoneda, *J. Electrochem. Soc.* **1997**, *144*, 2495; c) L. Kimerling, J. Patel, *Appl. Phys. Lett.* **1979**, *34*, 73.
[18] a) F. Cavallo, W. Sigle, O. G. Schmidt, *J. Appl. Phys.* **2008**, *103*, 116103; b) S. V. Golod, V. Y. Prinz, P. Wägli, L. Zhang, O. Kirfel, E. Deckhardt, F. Glaus, C. David, D. Grützmacher, *Appl. Phys. Lett.* **2004**, *84*, 3391.
[19] a) J. Chung, L. Rabenberg, *Ultramicroscopy* **2008**, *108*, 1595; b) J. Chung, G. Lian, L. Rabenberg, *IEEE Electron Device Lett.* **2010**, *31*, 854.
[20] G. P. Nikishkov, *J. Appl. Phys.* **2003**, *94*, 5333.
[21] a) N. Ma, D. Jena, *Phys. Rev. X* **2014**, *4*, 011043; b) Y. Zhang, V. W. Brar, C. Girit, A. Zettl, M. F. Crommie, *Nat. Phys.* **2009**, *5*, 722.
[22] a) T. Ando, A. B. Fowler, F. Stern, *Rev. Mod. Phys.* **1982**, *54*, 437; b) C. H. Gan, J. A. d. Alamo, B. R. Bennett, B. S. Meyerson, E. F. Crabbe, C. G. Sodini, L. R. Reif, *IEEE Trans. Electron Devices* **1994**, *41*, 2430.
[23] R. H. Kingston, *J. Appl. Phys.* **1956**, *27*, 101.
[24] a) H. Lee, D. H. Lee, T. Kanashima, M. Okuyama, *Appl. Surf. Sci.* **2008**, *254*, 6932; b) E. Yablonovitch, D. L. Allara, C. C. Chang, T. Gmitter, T. B. Bright, *Phys. Rev. Lett.* **1986**, *57*, 249.
[25] a) A. Pirkle, J. Chan, A. Venugopal, D. Hinojos, C. W. Magnuson, S. McDonnell, L. Colombo, E. M. Vogel, R. S. Ruoff, R. M. Wallace, *Appl. Phys. Lett.* **2011**, *99*, 122108; b) E. Mercado, J. Anaya, M. Kuball, *ACS Appl. Mater. Interfaces* **2021**, *13*, 17910.
[26] E. J. Ryder, *Phys. Rev.* **1953**, *90*, 766.
[27] a) H. E. Romero, N. Shen, P. Joshi, H. R. Gutierrez, S. A. Tadigadapa, J. O. Sofo, P. C. Eklund, *ACS Nano* **2008**, *2*, 2037; b) B. Huang, Z. Li, Z. Liu, G. Zhou, S. Hao, J. Wu, B.-L. Gu, W. Duan, *J. Phys. Chem. C* **2008**, *112*, 13442.
[28] a) H. Luo, G. Yu, *Chem. Mater.* **2022**, *34*, 3588; b) M. Luo, *Phys. Rev. B* **2020**, *102*, 075421.
[29] R. R. Cloke, T. Marangoni, G. D. Nguyen, T. Joshi, D. J. Rizzo, C. Bronner, T. Cao, S. G. Louie, M. F. Crommie, F. R. Fischer, *JACS* **2015**, *137*, 8872.
[30] E. C. H. Wen, P. H. Jacobse, J. Jiang, Z. Wang, S. G. Louie, M. F. Crommie, F. R. Fischer, *JACS* **2023**, *145*, 19338.
[31] a) H. Fang, W. Hu, *Adv. Sci.* **2017**, *4*, 1700323; b) F. Wang, T. Zhang, R. Xie, A. Liu, F. Dai, Y. Chen, T. Xu, H. Wang, Z. Wang, L. Liao, J. Wang, P. Zhou, W. Hu, *Adv. Mater.* **2024**, *36*, 2301197.
[32] a) Z. Ge, N. Xu, Y. Zhu, K. Zhao, Y. Ma, G. Li, Y. Chen, *ACS Photonics* **2022**, *9*, 59; b) G. Konstantatos, *Nat. Commun.* **2018**, *9*, 5266; c) A. Li, Q. Chen, P. Wang, Y. Gan, T. Qi, P. Wang, F. Tang, J. Z. Wu, R. Chen, L. Zhang, Y. Gong, *Adv. Mater.* **2019**, *31*, 1805656; d) H. Jiang, J. Fu, J. Wei, S. Li, C. Nie, F. Sun, Q. Y. S. Wu, M. Liu, Z. Dong, X. Wei, W. Gao, C.-W. Qiu, *Nat. Commun.* **2024**, *15*, 1225; e) U. N. Noumbé, C. Gréboval, C. Livache, A. Chu, H. Majjad, L. E. Parra López, L. D. N. Mouafo, B. Doudin, S. Berciaud, J. Chaste, A. Ouerghi, E. Lhuillier, J.-F. Dayen, *ACS Nano* **2020**, *14*, 4567; f) C.-H. Lee, G.-H. Lee, A. M. van der Zande, W. Chen, Y. Li, M. Han, X. Cui, G. Arefe, C. Nuckolls, T. F. Heinz, J. Guo, J. Hone, P. Kim, *Nat. Nanotechnol.* **2014**, *9*, 676; g) Y. Xiong, Q. Liao, Z. Huang, X. Huang, C. Ke, H. Zhu, C. Dong, H. Wang, K. Xi, P. Zhan, F. Xu, Y. Lu, *Adv. Mater.* **2020**, *32*, 1907242; h) J. Guo, J. Li, C. Liu, Y. Yin, W. Wang, Z. Ni, Z. Fu, H. Yu, Y. Xu, Y. Shi, Y. Ma, S. Gao, L. Tong, D. Dai, *Light Sci. Appl.* **2020**, *9*, 29; i) S. Cakmakyapan, P. K. Lu, A. Navabi, M. Jarrahi, *Light Sci. Appl.* **2018**, *7*, 20.
[33] G. Henkelman, A. Arnaldsson, H. Jónsson, *Comput. Mater. Sci.* **2006**, *36*, 354.
[34] K. Momma, F. Izumi, *J. Appl. Crystallogr.* **2011**, *44*, 1272.
[35] a) J. Yin, H. Wang, H. Peng, Z. Tan, L. Liao, L. Lin, X. Sun, A. L. Koh, Y. Chen, H. Peng, Z. Liu, *Nat. Commun.* **2016**, *7*, 10699; b) M. M. Monshi, S. M. Aghaei, I. Calizo, *Phys. Lett. A* **2018**, *382*, 1171.

[36] a) J. Vučić, C. Kottke, S. Nerreter, K.-D. Langer, J. W. Walewski, *J. Lightwave Technol.* **2010**, *28*, 3512; b) L. Nadal, M. S. Moreolo, J. M. Fàbrega, A. Dochhan, H. Grießer, M. Eiselt, J.-P. Elbers, *J. Lightwave Technol.* **2014**, *32*, 4143.
[37] a) Z. Li, R. J. Young, I. A. Kinloch, N. R. Wilson, A. J. Marsden, A. P. A. Raju, *Carbon* **2015**, *88*, 215; b) G. Heo, Y. S. Kim, S.-H. Chun, M.-J. Seong, *Nanoscale Res. Lett.* **2015**, *10*, 45.
[38] R. Legtenberg, H. Jansen, M. de Boer, M. Elwenspoek, *J. Electrochem. Soc.* **1995**, *142*, 2020.
[39] G. Kresse, J. Furthmüller, *Phys. Rev. B* **1996**, *54*, 11169.
[40] G. Kresse, D. Joubert, *Phys. Rev. B* **1999**, *59*, 1758.
[41] J. P. Perdew, K. Burke, M. Ernzerhof, *Phys. Rev. Lett.* **1996**, *77*, 3865.
[42] V. Wang, N. Xu, J.-C. Liu, G. Tang, W.-T. Geng, *Comput. Phys. Commun.* **2021**, *267*, 108033.